

Article

Impacts of Residual Stress on Micro Vibratory Platform Used for Inertial Sensor Calibration

Rui Hao, Huijun Yu, Bei Peng, Haixiang Zhan and Wu Zhou * 

School of Mechanical and Electrical Engineering, University of Electronic Science and Technology of China, Chengdu 611731, China; hr1351440347@std.uestc.edu.cn (R.H.); yuhjuestc@126.com (H.Y.); beipeng@uestc.edu.cn (B.P.); zhanhaixiang@163.com (H.Z.)

* Correspondence: zhouwu916@uestc.edu.cn; Tel.: +86-1588-2211-305

Received: 11 May 2020; Accepted: 14 July 2020; Published: 16 July 2020



Abstract: A micro vibratory platform driven by converse piezoelectric effects is a promising in-situ recalibration platform to eliminate the influence of bias and scale factor drift caused by long-term storage of micro-electro-mechanical system (MEMS) inertial sensors. The calibration accuracy is critically determined by the stable and repeatable vibration of platform, and it is unavoidably impacted by the residual stress of micro structures and lead zirconate titanate (PZT) hysteresis. The abnormal phenomenon of the observed displacement response in experiments was investigated analytically using the stiffness model of beams and hysteresis model of piezoelectric material. Rather than the hysteresis, the initial deflection formed by the residual stress of the beam was identified as the main cause of the response error around the zero position. This conclusion provides guidelines to improve the performance and control of micro vibratory platforms.

Keywords: micro vibratory platform; inertial sensor calibration; residual stress; PZT hysteresis

1. Introduction

Micro-electro-mechanical system (MEMS) inertial sensors are widely used in the aerospace field [1] and in intelligent robots [2]. However, its bias and scale factor drift caused by temperature [3] and long-term storage [4,5] prevent its applications in highly precise fields [6]. Therefore, an in-situ and movable recalibration platform or method is much needed to suppress the drift without relying on fixed equipment [7] and strict environmental requirements [8]. To meet these requirements, a micro vibratory platform driven by converse piezoelectric effect was proposed to provide an inertial stimulus for both gyroscope [9] and accelerometer [10] calibration. Compared with the self-test structure that is usually used for evaluating the device performance [11], the vibratory platform can generate an accurate signal to quantitatively calibrate the bias and scale factor of sensors.

A multi-axis vibratory platform designed by a team at the University of Michigan for in situ self-calibration of general MEMS inertial sensors [12,13], which can achieve 150°/s angular rate and 0.3 g (1 g = 9.8 m/s²) linear acceleration. It is integrated with the commercial Invensense MPU-6500 (IMU) and is expected to provide the scale-factor calibration with estimation error <20 ppm, yet the capacitive position sensor for platform motion detection has temperature drift [14] and dielectric polarization effect [15]. After that, a team at Cornell University reported a new vibratory platform for gyroscope calibration [16], which adds an integrated optical metrology system and a CMOS (Complementary Metal Oxide Semiconductor) imager for closed loop control of the vibratory platform. The piezoelectric vibratory platform is capable of generating 0~300°/s angular rate for scale factor and bias measurement, and it has 0~90 m/s² in-plane acceleration to extract the gyroscope in-plane acceleration sensitivities. The additional optical metrology system can ensure the long-term stability of the vibratory platform at 10 ppm. In the same period, a team at the China Academy of Engineering Physics also reported a micro

vibratory platform with high dynamic for the in-situ calibration of inertial MEMS devices [17]; it can provide 16 g acceleration and 720°/s angular rate for 19 mg payload (a commercial 3-axis accelerometer H3LIS331DL).

However, due to the appearance of the residual stress of micro fabrication and the hysteresis effect [18,19] of piezoelectric material, the vibratory stage exhibited an initial displacement of 0~20 μm and an abnormal displacement response, which was obtained using an optical measurement system proposed in our previous work [20]. After that, the platform was optimized to gain a lower off-axis error less than 1% [21], but the improvement contributed little to reducing the error induced by residual stress and the hysteresis effect.

This study aimed to find out the underlying mechanism behind the abnormal z-axis displacement curve of the platform test. The test results are shown in Section 2 to show which error needs to be studied, and Section 3 describes how the investigation was carried out in detail. In Section 4, the influence of residual stress on the vibratory platform displacement response is discussed farther. Finally, a conclusion is included in Section 5.

2. Platform Test

The optical test method [20] and fabrication [21] of a vibratory platform were reported in recent work. The measurement principle is as follows. It consists of a central vertical cavity surface emitting laser (VCSEL) and several photodiodes (PDs); when the vibratory platform vibrates along the z-axis, the relative movement between the vibratory platform surface and the light receiving surface of optical measurement system affects the intensity of reflected light from VCSEL. Then, the reflected lights can be extracted by the PDs array to achieve accurate motion perception and estimation (Figure 1).

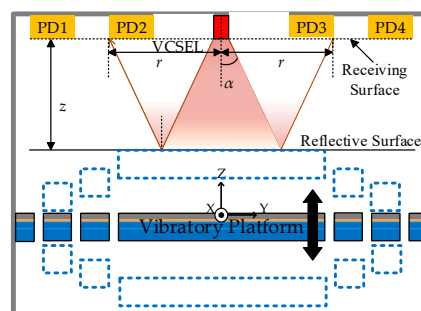


Figure 1. Schematic diagram of the optical measurement system.

The vibratory platform is shown in Figure 2. It consists of a rigid stage supported by four L-shape beams which were constructed using a silicon structure layer, a lead zirconate titanate (PZT) drive layer, and two metal electrode layers. The movement along the z-axis was actuated by a designed combination of positive voltage on the inner parts and negative voltage on the outer parts.

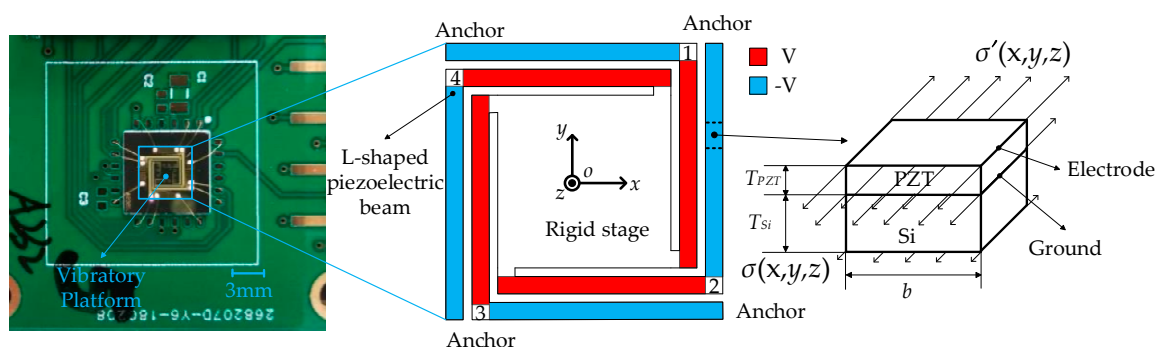


Figure 2. Piezoelectric vibratory platform.

The excitation voltage was a sinusoidal signal with an amplitude of 8 V and frequency of 317 Hz. The test results indicate an obvious offset near the zero point of displacement in Figure 3a, and when different voltages with amplitudes from 3 V to 9 V were applied to acquire the amplitude-frequency curves, an increase of resonant frequency of stage from 500 Hz to 510 Hz appeared, as shown in Figure 3b. The abnormal phenomenon could be induced from the residual stress [22] in each L-shape beam, as shown the right side of Figure 1, PZT hysteresis, or both [23]. The following will describe our investigation of the influence of both mechanisms.

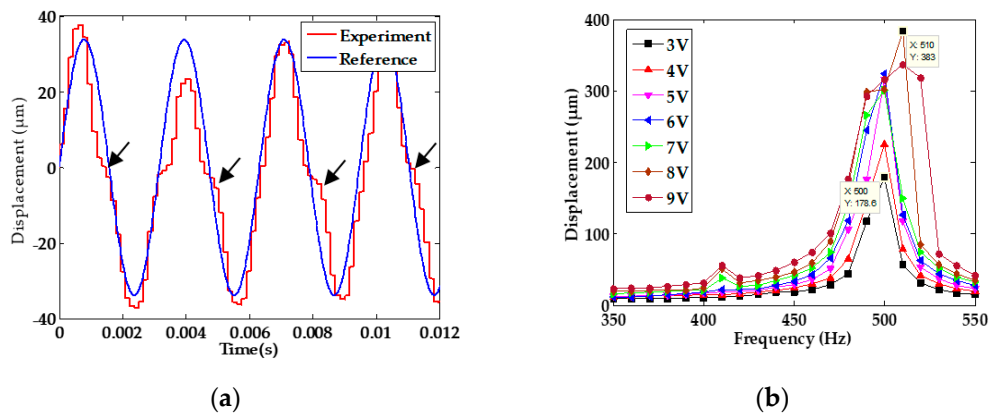


Figure 3. (a) Displacement response with abnormal phenomenon; (b) amplitude-frequency characteristic.

3. Investigation of the Abnormal Phenomenon

3.1. Influence of Residual Stress

The residual stress of the beam for supporting the vibratory platform is caused by the micro fabrication processes, like deposition, etching, sputtering, releasing, and so on. It induces an initial displacement of the vibratory platform. Before that, the four L-shaped beam of the MEMS micro vibratory platform are connected with each other to form a closed ring beam. The relationship between each part can be seen in Figure 4.

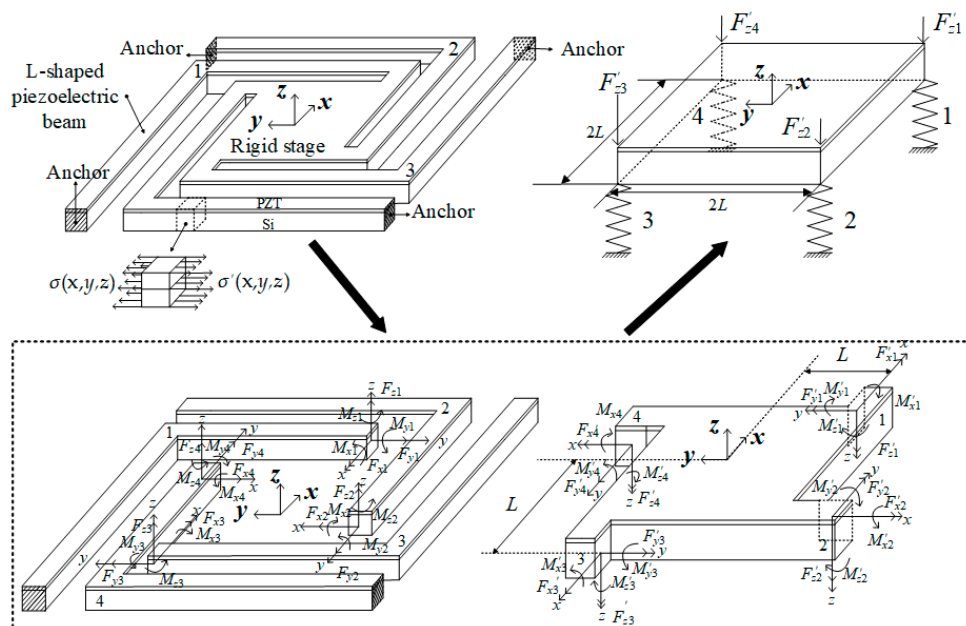


Figure 4. The relationship between rigid stage and four L-shaped beams.

The vibratory platform can be parted with four L-shaped beams and a rigid stage. The in-plane deformation of the beam is negligible when compared to the out-of-plane deformation. Due to the symmetry of structure and load, only one single L-shape beam needs to be modeled. One end of beam fixed on the substrate had the boundary condition of all the displacement and rotation equal to zero, and the other end, connecting to the stage, has a zero rotation and a single translation freedom along z -axis, called a guided boundary condition [24,25].

Because of the elastic deformation of materials, the stress gradient is linear within each layer of L-shaped beam [26]. The stress in the top and bottom layer of the beam is assumed to be σ_1 and σ_3 , and the stress at the interface between the piezoelectric layer and the silicon layer is σ_2 (Figure 5).

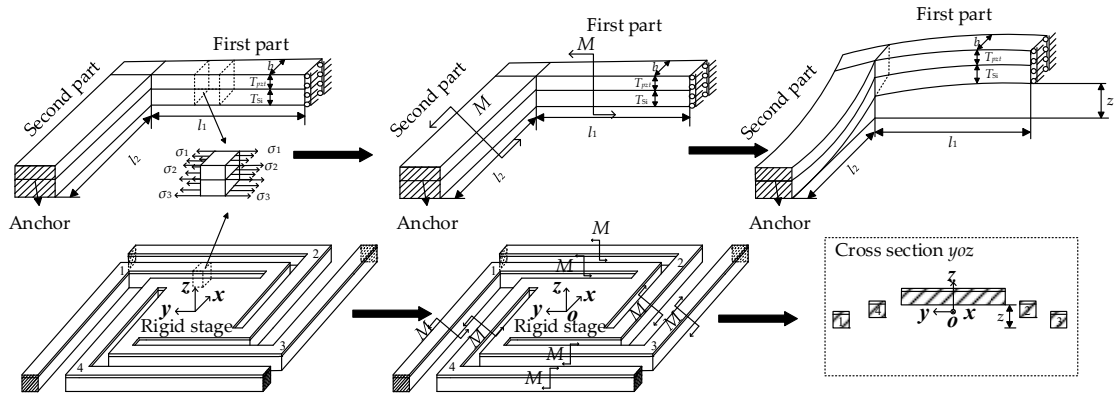


Figure 5. Deformation diagram of L-shaped piezoelectric micro beam and vibratory platform with inside residual stress.

The total stress of beam expresses can be expressed as:

$$stress = \frac{\sigma_1 + \sigma_2}{2} \frac{T_{PZT}}{T_{PZT} + T_{Si}} + \frac{\sigma_2 + \sigma_3}{2} \frac{T_{Si}}{T_{PZT} + T_{Si}} + (\sigma_1 - \sigma_2) \frac{z - T_{Si}}{T_{PZT}} \Big|_{T_{Si} \leq z \leq T_{PZT} + T_{Si}} + (\sigma_2 - \sigma_3) \frac{z}{T_{Si}} \Big|_{0 \leq z < T_{Si}}, \quad (1)$$

where the T_{PZT} and T_{Si} represent the thickness of PZT layer and Si layer, respectively. The bottom of the beam as the zero point of the z coordinate. The uniform stress (the first two items in Equation (1)), $T_{PZT}(\sigma_1 + \sigma_2)/(2(T_{PZT} + T_{Si})) + T_{Si}(\sigma_2 + \sigma_3)/(2(T_{PZT} + T_{Si}))$ accounts for the in-plane elongation of the beam, whereas the $(\sigma_1 - \sigma_2)((z - T_{Si})/T_{PZT}) + (\sigma_2 - \sigma_3)(z/T_{Si})$ (the stress gradient component, the last two items in Equation (1)) causes out-of-plane deflection. The equivalent bending moment due to residual stress can be written as:

$$\begin{aligned} M &= \int_0^{T_{PZT} + T_{Si}} dM \\ &= \int_{T_{Si}}^{T_{PZT} + T_{Si}} (\sigma_1 - \sigma_2) \frac{b(z - T_{Si})^2}{T_{PZT}} dz + \int_0^{T_{Si}} (\sigma_2 - \sigma_3) \frac{bz^2}{T_{Si}} dz \\ &= \frac{b(\sigma_1 - \sigma_2)}{T_{PZT}} \left(\frac{(T_{PZT} + T_{Si})^3}{3} - T_{PZT}^2 T_{Si} - T_{PZT} T_{Si}^2 \right) + \frac{b(\sigma_2 - \sigma_3) T_{Si}^3}{3}, \end{aligned} \quad (2)$$

where b is the width of beam. The equivalent bending moment, M , is a linear combination of stress gradient due to residual stress. Then, a beam theory was used to calculate the beam initial deflection [27] by:

$$EI \frac{d^2 z(y)}{dy^2} = M, \quad (3)$$

$$z(y) = \left[\frac{b(\sigma_1 - \sigma_2)}{T_{PZT}} \left(\frac{(T_{PZT} + T_{Si})^3}{3} - T_{PZT}^2 T_{Si} - T_{PZT} T_{Si}^2 \right) + \frac{b(\sigma_2 - \sigma_3) T_{Si}^3}{3} \right] \frac{y^2}{EI} + C_1 y + C_2, \quad (4)$$

where the C_1 and C_2 are decided by specific boundary conditions. Substituting $y = l_i$, (l_i is the length of i -th part of each L-shaped beam) into Equation (4), the initial deflection of the beam can be expressed as:

$$z_{initial}(l_i) = (\sigma_1 - \sigma_2) \left[\frac{bl^2}{T_{PZT}EI} \left(\frac{(T_{PZT} + T_{Si})^3}{3} - T_{PZT}^2 T_{Si} - T_{PZT} T_{Si}^2 \right) \right] + (\sigma_2 - \sigma_3) \left[\frac{bl^2}{T_{PZT}EI} \frac{T_{Si}^3}{3} \right] + C_1 l_i + C_2. \tag{5}$$

The initial deflection $z_{initial}(l_i)$ of the piezoelectric micro beam is a linear combination of residual stress gradient and $z = z_{initial}(l_1) + z_{initial}(l_2)$. The obvious difference of curvatures of two segments results from the distinguished load and end constraints. Thus, the residual stress is replaced by the initial deflection z to investigate the impacts of displacement response (Figure 6).

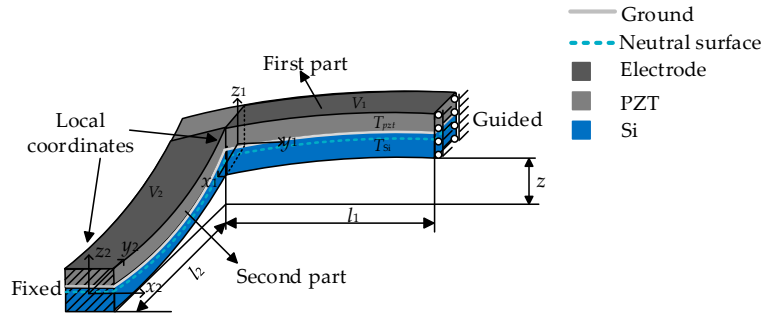


Figure 6. L-shaped micro beam diagram with the initial deflection z .

The L-shaped beam is divided into two segments for a simple analysis. When one segment is considered, the other is treated as a rigid body. The guided boundary can be replaced by a set of $F_x, F_y, F_z, M_x, M_y,$ and M_z , and the $F_{xi}, F_{yi}, F_{zi}, M_{xi}, M_{yi},$ and M_{zi} represent the set of force and moment at the end of each part of the L-shaped beam respectively, where the subscript i indicates the i -th part of L-shaped beam (Figure 7).

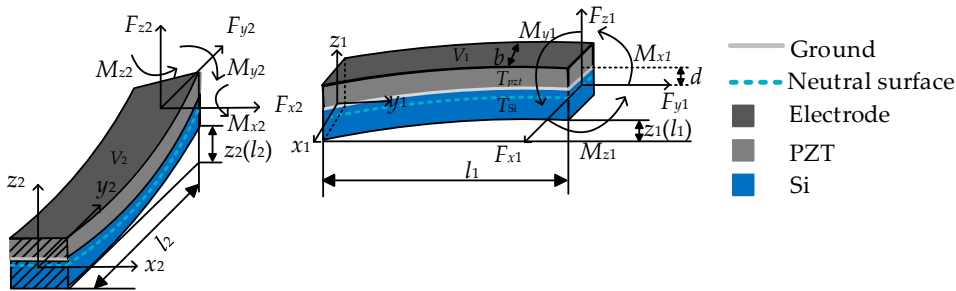


Figure 7. Diagram of each segment beam.

The relationship between $F_x, F_y, F_z, M_x, M_y, M_z$ and $F_{xi}, F_{yi}, F_{zi}, M_{xi}, M_{yi},$ and M_{zi} are shown in Equation (6):

$$\begin{aligned} F_{x1} &= F_x, F_{y1} = F_y, F_{z1} = F_z, M_{x1} = M_x, M_{y1} = M_y, M_{z1} = M_z \\ F_{x2} &= F_y, F_{y2} = -F_x, F_{z2} = F_z, M_{x2} = M_y, M_{y2} = -M_x + F_z l_1, M_{z2} = M_z - F_x l_1 \end{aligned} \tag{6}$$

The stiffness, F_z/z , is regarded as the solution by the following constraints at the corner of the L-shaped beam in Equation (7).

$$x_1(0) = y_2(l_2), y_1(0) = x_2(l_2), z_1(0) = z_2(l_2), \theta_{x1}(0) = -\theta_{y2}(l_2), \theta_{y1}(0) = \theta_{x2}(l_2), \theta_{z1}(0) = \theta_{z2}(l_2), \tag{7}$$

where x_i, y_i and z_i represent the displacement of the i -th part on the x -axis, y -axis, and z -axis, respectively. θ_{xi}, θ_{yi} and θ_{zi} represent the angle of the i -th part around the x -axis, y -axis, and z -axis, respectively. Then, the differential equation of deflection is given by [28] as:

$$EI_i \frac{d^2 z_i(y_i)}{dy_i^2} = F_{zi}(l_i - y_i) + M_{xi} - dE_{pzt}bd_{31}V_i - F_{yi}[z_i(l_i) - z_i(y_i)], \tag{8}$$

In Equation (8), the E_{pzt} is the elastic modulus of PZT. EI_i is the flexural rigidity. d is the distance between the PZT layer center coordinate and the neutral surface. b is the width of beam, and d_{31} is the piezoelectric coefficient [29]. V_i is the driving voltage.

The solution of the differential equation is shown in Equations (9) and (10):

$$z_i(y_i)|_{\alpha_{i1} < 0} = C_{i1} \frac{F_{zi}}{EI_i} \cos(\sqrt{-\alpha_{i1}}y_i) + C_{i2} \frac{F_{zi}}{EI_i} \sin(\sqrt{-\alpha_{i1}}y_i) + \frac{\frac{F_{zi}}{EI_i}y_i - \alpha_{i1}z_i(l_i) - \frac{F_{zi}}{EI_i}l_i - C_{i3}}{-\alpha_{i1}}, \tag{9}$$

$$z_i(y_i)|_{\alpha_{i1} > 0} = C_{i1} \frac{F_{zi}}{EI_i} e^{\sqrt{\alpha_{i1}}y_i} + C_{i2} \frac{F_{zi}}{EI_i} e^{-\sqrt{\alpha_{i1}}y_i} + \frac{\frac{F_{zi}}{EI_i}y_i + \alpha_{i1}z_i(l_i) - \frac{F_{zi}}{EI_i}l_i - C_{i3}}{\alpha_{i1}}, \tag{10}$$

where $\alpha_{i1} = F_{yi}/EI_i$, the unknown coefficients C_{i1}, C_{i2} , and C_{i3} were listed in Table 1, parameter k_{ri} is the torsional stiffness of the i -th part.

Table 1. The coefficients of Equations (9) and (10).

Coefficient	Expression
$\alpha_{11} < 0, C_{11}$	$\frac{(\cos(\sqrt{-\alpha_{11}}l_1) - 1)}{-\alpha_{11}^{3/2} \left(\sin(\sqrt{-\alpha_{11}}l_1) + \frac{EI_1}{k_{r1}} \sqrt{-\alpha_{11}} \cos(\sqrt{-\alpha_{11}}l_1) \right)}$
$\alpha_{11} < 0, C_{12}$	$\frac{\left(\sin(\sqrt{-\alpha_{11}}l_1) + \frac{EI_1}{k_{r1}} \sqrt{-\alpha_{11}} \right)}{-\alpha_{11}^{3/2} \left(\sin(\sqrt{-\alpha_{11}}l_1) + \frac{EI_1}{k_{r1}} \sqrt{-\alpha_{11}} \cos(\sqrt{-\alpha_{11}}l_1) \right)}$
$\alpha_{11} < 0, C_{13}$	$\frac{\frac{F_{z1}}{EI_1} (1 - \cos(\sqrt{-\alpha_{11}}l_1)) - \sqrt{-\alpha_{11}}l_1 \sin(\sqrt{-\alpha_{11}}l_1) - (-\alpha_{11})l_1 \frac{EI_1}{k_{r1}} \cos(\sqrt{-\alpha_{11}}l_1)}{-\alpha_{11}^{1/2} \left(\sin(\sqrt{-\alpha_{11}}l_1) + \frac{EI_1}{k_{r1}} \sqrt{-\alpha_{11}} \cos(\sqrt{-\alpha_{11}}l_1) \right)}$ $+ z_1(l_1) \frac{-\alpha_{11}^{3/2} \sin(\sqrt{-\alpha_{11}}l_1) + \alpha_{11}^2 \frac{EI_1}{k_{r1}} \cos(\sqrt{-\alpha_{11}}l_1)}{-\alpha_{11}^{1/2} \left(\sin(\sqrt{-\alpha_{11}}l_1) + \frac{EI_1}{k_{r1}} \sqrt{-\alpha_{11}} \cos(\sqrt{-\alpha_{11}}l_1) \right)}$
$\alpha_{21} < 0, C_{21}$	$\frac{(1 - \cos(\sqrt{-\alpha_{21}}l_2)) + \sqrt{-\alpha_{21}} \frac{EI_2}{k_{r2}} \sin(\sqrt{-\alpha_{21}}l_2)}{-\alpha_{21}^{3/2} \left(\sin(\sqrt{-\alpha_{21}}l_2) + \frac{EI_2}{k_{r2}} \sqrt{-\alpha_{21}} \cos(\sqrt{-\alpha_{21}}l_2) \right)}$
$\alpha_{21} < 0, C_{22}$	$\frac{1}{-\alpha_{21}^{3/2}}$
$\alpha_{21} < 0, C_{23}$	$\frac{\frac{F_{z2}}{EI_2} \left[\begin{aligned} & \frac{(1 - \cos(\sqrt{-\alpha_{21}}l_2)) + \sqrt{-\alpha_{21}} \frac{EI_2}{k_{r2}} \sin(\sqrt{-\alpha_{21}}l_2)}{-\alpha_{21}^{1/2} \left(\sin(\sqrt{-\alpha_{21}}l_2) + \frac{EI_2}{k_{r2}} \sqrt{-\alpha_{21}} \cos(\sqrt{-\alpha_{21}}l_2) \right)} \\ & - \frac{\sqrt{-\alpha_{21}}l_2 \sin(\sqrt{-\alpha_{21}}l_2) + (-\alpha_{21})l_2 \frac{EI_2}{k_{r2}} \cos(\sqrt{-\alpha_{21}}l_2)}{-\alpha_{21}^{1/2} \left(\sin(\sqrt{-\alpha_{21}}l_2) + \frac{EI_2}{k_{r2}} \sqrt{-\alpha_{21}} \cos(\sqrt{-\alpha_{21}}l_2) \right)} \end{aligned} \right]}{-\alpha_{21}^{3/2} \sin(\sqrt{-\alpha_{21}}l_2) + \alpha_{21}^2 \frac{EI_2}{k_{r2}} \cos(\sqrt{-\alpha_{21}}l_2)}$ $+ z_2(l_2) \frac{-\alpha_{21}^{1/2} \left(\sin(\sqrt{-\alpha_{21}}l_2) + \frac{EI_2}{k_{r2}} \sqrt{-\alpha_{21}} \cos(\sqrt{-\alpha_{21}}l_2) \right)}{-\alpha_{21}^{1/2} \left(\sin(\sqrt{-\alpha_{21}}l_2) + \frac{EI_2}{k_{r2}} \sqrt{-\alpha_{21}} \cos(\sqrt{-\alpha_{21}}l_2) \right)}$
$\alpha_{11} > 0, C_{11}$	$\frac{e^{\sqrt{\alpha_{11}}l_1} - 1 + \sqrt{\alpha_{11}} \frac{EI_1}{k_{r1}} e^{\sqrt{\alpha_{11}}l_1}}{\alpha_{11}^{3/2} \left(e^{2\sqrt{\alpha_{11}}l_1} + \sqrt{\alpha_{11}} \frac{EI_1}{k_{r1}} + \sqrt{\alpha_{11}} \frac{EI_1}{k_{r1}} e^{2\sqrt{\alpha_{11}}l_1} - 1 \right)}$
$\alpha_{11} > 0, C_{12}$	$\frac{e^{\sqrt{\alpha_{11}}l_1} \left(e^{\sqrt{\alpha_{11}}l_1} + \sqrt{\alpha_{11}} \frac{EI_1}{k_{r1}} - 1 \right)}{\alpha_{11}^{3/2} \left(e^{2\sqrt{\alpha_{11}}l_1} + \sqrt{\alpha_{11}} \frac{EI_1}{k_{r1}} + \sqrt{\alpha_{11}} \frac{EI_1}{k_{r1}} e^{2\sqrt{\alpha_{11}}l_1} - 1 \right)}$

Table 1. Cont.

Coefficient	Expression
$\alpha_{11} > 0, C_{13}$	$\frac{F_{z1}}{EI_1} \frac{1 + \sqrt{\alpha_{11}l_1} - 2e^{\sqrt{\alpha_{11}l_1}} + e^{2\sqrt{\alpha_{11}l_1}} - \sqrt{\alpha_{11}l_1}e^{2\sqrt{\alpha_{11}l_1}} - \alpha_{11}l_1 \frac{EI_1}{k_1} - \alpha_{11}l_1 \frac{EI_1}{k_1} e^{2\sqrt{\alpha_{11}l_1}}}{\sqrt{\alpha_{11}} \left(e^{2\sqrt{\alpha_{11}l_1}} + \sqrt{\alpha_{11} \frac{EI_1}{k_1}} + \sqrt{\alpha_{11} \frac{EI_1}{k_1}} e^{2\sqrt{\alpha_{11}l_1}} - 1 \right)}$ $+ z_1(l_1) \frac{\alpha_{11}^{3/2} (1 - e^{2\sqrt{\alpha_{11}l_1}}) + \alpha_{11}^2 \frac{EI_1}{k_1} + \alpha_{11}^2 \frac{EI_1}{k_1} e^{2\sqrt{\alpha_{11}l_1}}}{\sqrt{\alpha_{11}} \left(e^{2\sqrt{\alpha_{11}l_1}} + \sqrt{\alpha_{11} \frac{EI_1}{k_1}} + \sqrt{\alpha_{11} \frac{EI_1}{k_1}} e^{2\sqrt{\alpha_{11}l_1}} - 1 \right)}$
$\alpha_{21} > 0, C_{21}$	$- \frac{\alpha_{21}^{3/2} \left(e^{2\sqrt{\alpha_{21}l_2}} + \sqrt{\alpha_{21} \frac{EI_2}{k_2}} + \sqrt{\alpha_{21} \frac{EI_2}{k_2}} e^{2\sqrt{\alpha_{21}l_2}} - 1 \right)}{e^{2\sqrt{\alpha_{21}l_2}} - e^{\sqrt{\alpha_{21}l_2}} + \sqrt{\alpha_{21} \frac{EI_2}{k_2}} e^{2\sqrt{\alpha_{21}l_2}}}$
$\alpha_{21} > 0, C_{22}$	$\frac{\alpha_{21}^{3/2} \left(e^{2\sqrt{\alpha_{21}l_2}} + \sqrt{\alpha_{21} \frac{EI_2}{k_2}} + \sqrt{\alpha_{21} \frac{EI_2}{k_2}} e^{2\sqrt{\alpha_{21}l_2}} - 1 \right)}{e^{2\sqrt{\alpha_{21}l_2}} - e^{\sqrt{\alpha_{21}l_2}} + \sqrt{\alpha_{21} \frac{EI_2}{k_2}} e^{2\sqrt{\alpha_{21}l_2}}}$
$\alpha_{21} > 0, C_{23}$	$\frac{F_{z2}}{EI_2} \frac{(e^{\sqrt{\alpha_{21}l_2}} - 1)^2 + \sqrt{\alpha_{21} \frac{EI_2}{k_2}} (e^{2\sqrt{\alpha_{21}l_2}} - 1) - \sqrt{\alpha_{21}l_2} (e^{2\sqrt{\alpha_{21}l_2}} - 1) + \alpha_{21}l_2 \frac{EI_2}{k_2} (e^{2\sqrt{\alpha_{21}l_2}} + 1)}{\sqrt{\alpha_{21}} \left(e^{2\sqrt{\alpha_{21}l_2}} + \sqrt{\alpha_{21} \frac{EI_2}{k_2}} + \sqrt{\alpha_{21} \frac{EI_2}{k_2}} e^{2\sqrt{\alpha_{21}l_2}} - 1 \right)}$ $+ z_2(l_2) \frac{\alpha_{21}^{3/2} (e^{2\sqrt{\alpha_{21}l_2}} - 1) + \alpha_{21}^2 \frac{EI_2}{k_2} (e^{2\sqrt{\alpha_{21}l_2}} + 1)}{\sqrt{\alpha_{21}} \left(e^{2\sqrt{\alpha_{21}l_2}} + \sqrt{\alpha_{21} \frac{EI_2}{k_2}} + \sqrt{\alpha_{21} \frac{EI_2}{k_2}} e^{2\sqrt{\alpha_{21}l_2}} - 1 \right)}$

For brevity, the unknown coefficient C_{i3} can be abbreviated as $C_{i3} = A_{i3} F_{zi}/EI_i + B_{i3} z_i(l_i)$. Substituting $y_i = l_i$ into Equations (9) and (10), the result can be expressed in Equation (11).

$$\begin{cases} \frac{F_{zi}}{z_i} \Big|_{F_{yi}>0} = B_{i3} \left[\alpha_{i1} \left(\frac{C_{i1}}{EI_i} e^{\sqrt{\alpha_{i1}l_i}} + \frac{C_{i2}}{EI_i} e^{-\sqrt{\alpha_{i1}l_i}} - \frac{A_{i3}}{EI_i \alpha_{i1}} \right) \right]^{-1} \\ \frac{F_{zi}}{z_i} \Big|_{F_{yi}<0} = B_{i3} \left[\alpha_{i1} \left(\frac{C_{i1}}{EI_i} \cos(\sqrt{-\alpha_{i1}l_i}) + \frac{C_{i2}}{EI_i} \sin(\sqrt{-\alpha_{i1}l_i}) - \frac{A_{i3}}{EI_i \alpha_{i1}} \right) \right]^{-1} \end{cases} \quad (11)$$

It can be seen that Equation (11) is a piecewise function ($\alpha_{i1} = F_{yi}/EI_i$); it is related to the axial force F_{yi} which is determined by the beam initial deflection z , vibration displacement, and driving voltage. The relationship between stiffness and displacement under different voltages is depicted in Figure 8.

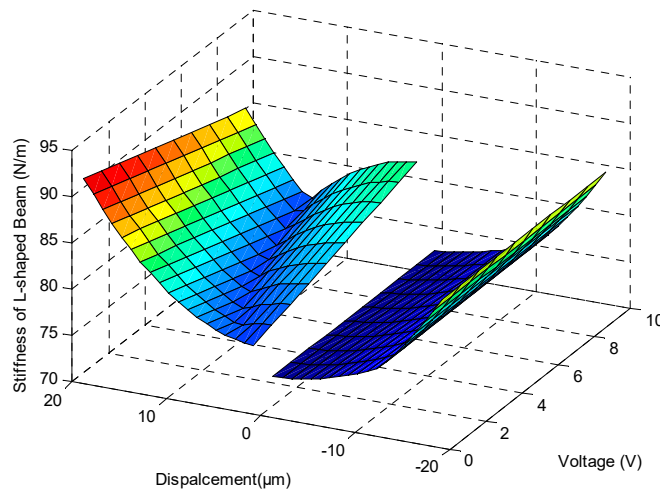


Figure 8. Stiffness of L-shaped piezoelectric beam.

There was a sharp increase of stiffness around zero displacement, because the axial force, F_{yi} , changed from a compressive state of negative displacement to a tensile state of positive displacement due to the residual stress. The level of stiffness variation is also related to the driving voltage as the internal stress level results from the piezoelectric layer deformation. The stiffening effect also appeared in the stage of large deformation of the beam and lead to a higher frequency of the vibratory platform.

3.2. Modeling PZT Hysteresis

The PZT hysteresis is another factor possibly resulting in a displacement error. The hysteretic behavior of piezoelectric material under the voltage stimulus is reported in [30,31]. To model this mechanism, the polynomial-based hysteresis model is simple and suitable to analyze the dynamic response of the system [32,33], which can be expressed as Equation (12):

$$f(E) = d_{ij}E - \eta E^3 + \frac{\zeta}{\omega^3} \dot{E}^3, \quad (12)$$

where the $f(E)$ is the hysteresis loop function. d_{ij} is the piezoelectric coefficient. E is the electric field, and ω is the frequency. The parameters η and ζ are the fitting parameters determining the shape of the hysteresis loop (Figure 9).

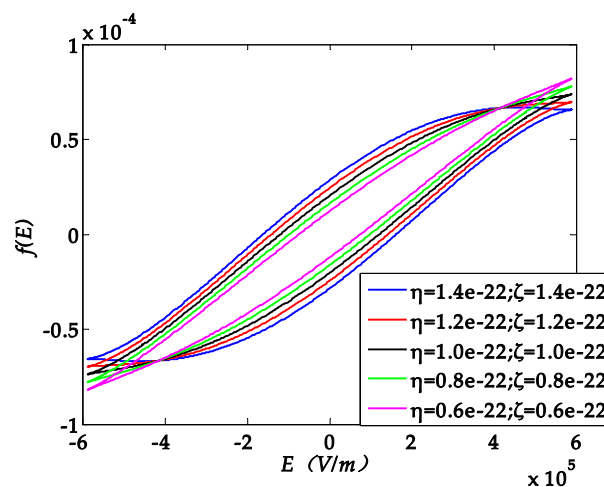


Figure 9. Hysteresis loop function with different parameters η and ζ .

In this example, the electric field is $E = V_{max} \sin(\omega t)/T_{PZT}$, where V_{max} is the maximum amplitude of voltage, 10 V, and T_{PZT} is the thickness of the piezoelectric layer, 17 μm . The hysteresis loop function $f(E)$ is described as the scaling behavior [34] of hysteresis in PZT ceramic by different η and ζ .

3.3. Residual Stress vs. PZT Hysteresis

Based on the mechanisms described above and the electromechanical coupling model reported in previous work, the commercial software Simulink was utilized to simulate the displacement response of vibratory platform. While the vibratory platform can be regarded as a mass-spring-damping system, and its vibration equation is shown in Equation (13).

$$M\ddot{z} + C\dot{z} + Kz = K_f \left(d_{ij}E - \eta E^3 + \frac{\zeta}{\omega^3} \dot{E}^3 \right), \quad (13)$$

where M and C represent the equivalent mass and damping coefficient separately, K is the stiffness in Equation (12). The right side of the equation represents the equivalent driving force which contains the hysteresis loop function, and the K_f is the coefficient. In Figure 10a,b show the influence of the residual stress and the PZT hysteresis, respectively. It indicates that the offset of the zero point is attributed to the residual stress and has almost nothing to do with the hysteresis of PZT materials (Figure 10b).

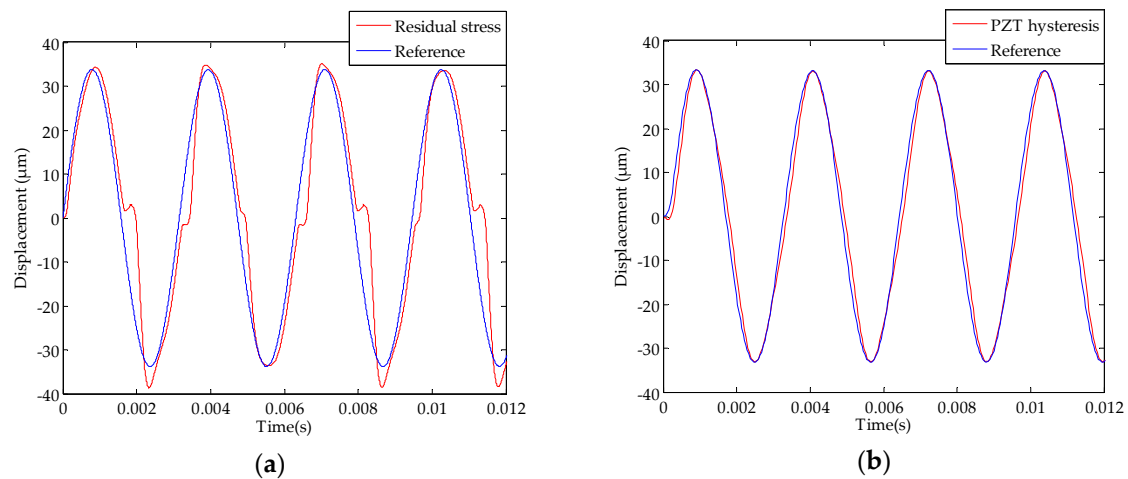


Figure 10. Displacement response simulation 8 V (317 Hz); (a) residual stress; (b) lead zirconate titanate (PZT) hysteresis.

For a comparison, Figure 11 considered both the residual stress and PZT hysteresis to investigate the impacts on the platform. The experiments and theoretical/simulation show agreement with each other.

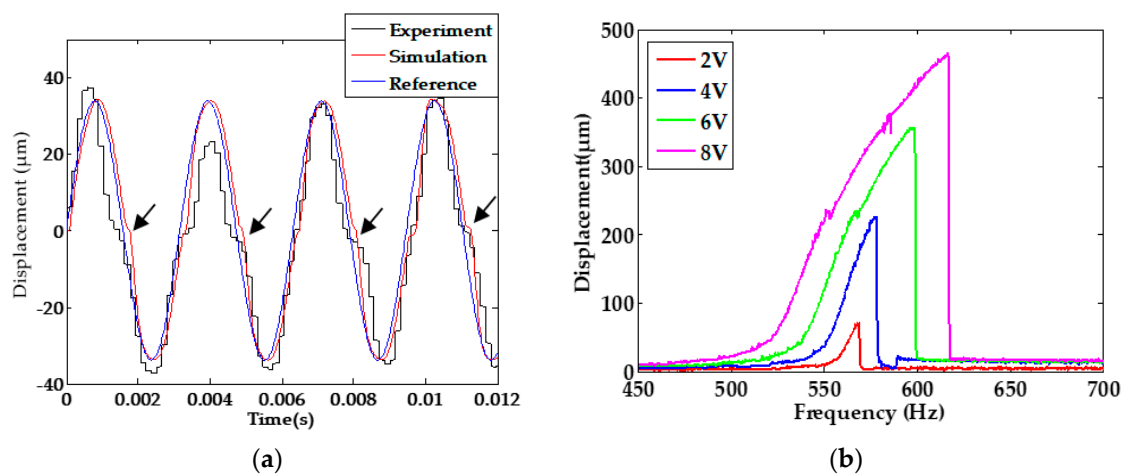


Figure 11. (a) Displacement response at sinusoidal excitation 8 V (317 Hz); (b) Amplitude-frequency response.

4. Discussion

In Section 3, the different stress gradient and load condition are discussed for the abnormal phenomena of the platform vibration. We set the linear stress gradient to ξ , and then the results of different stress gradients were simulated, as can be seen in Figure 12.

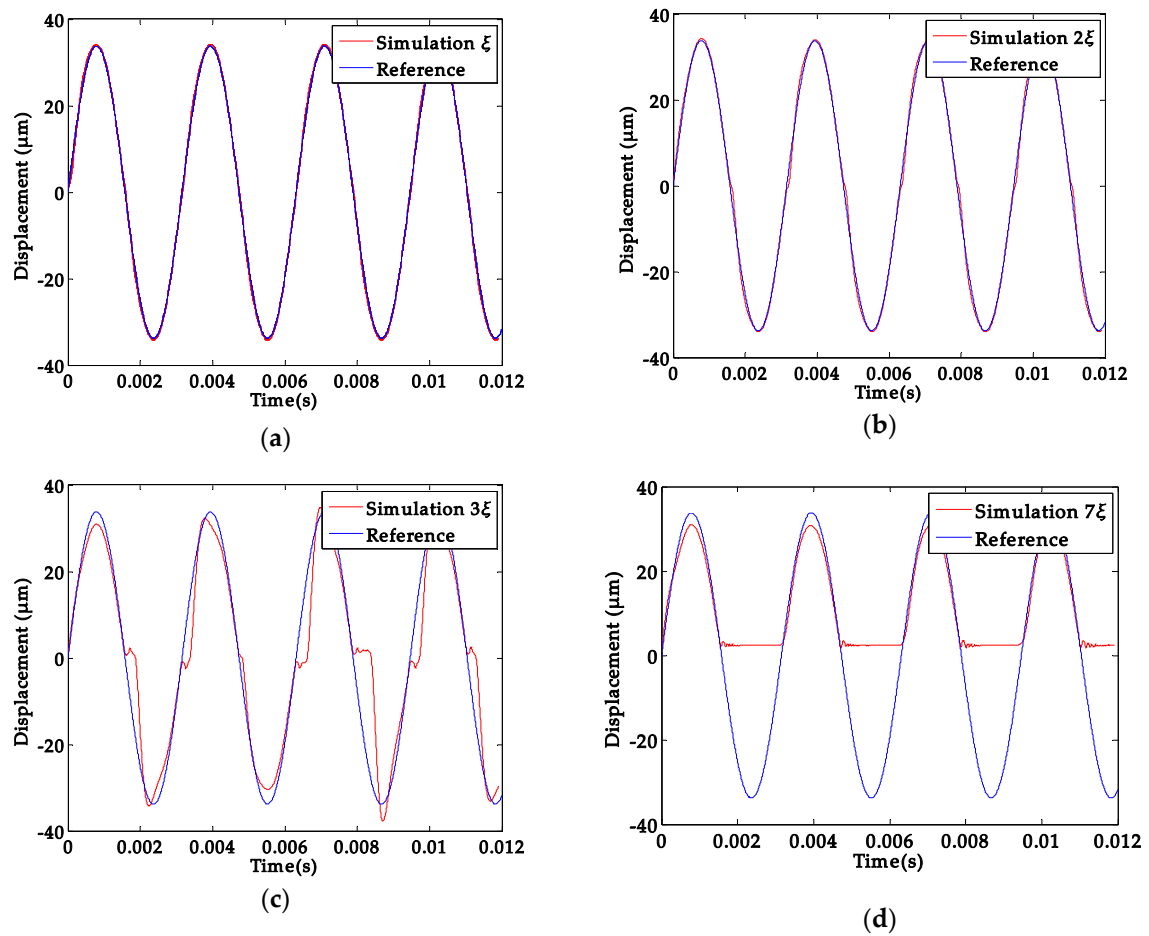


Figure 12. Displacement response simulation under different residual stress gradient 8 V (317 Hz); (a) ξ stress gradient; (b) 2ξ stress gradient; (c) 3ξ stress gradient; (d) 7ξ stress gradient.

The increase of the stress gradient caused the apparent abnormal phenomenon that can be seen in Figure 12. When the residual stress gradient increased to a certain level, the platform even failed (Figure 12d).

Moreover, whether the platform was loaded or not also affected the displacement response. The cases of unload or with a 40 mg load can be seen in Figure 13.

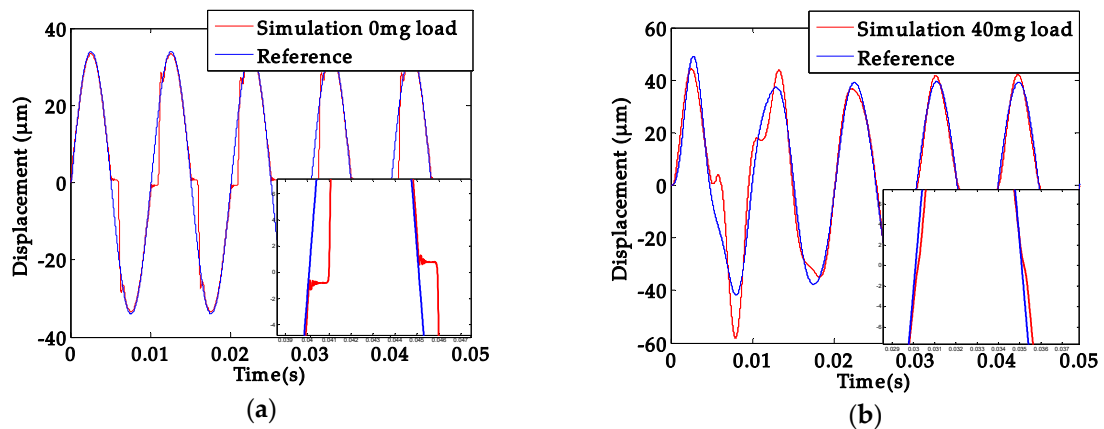


Figure 13. Cont.

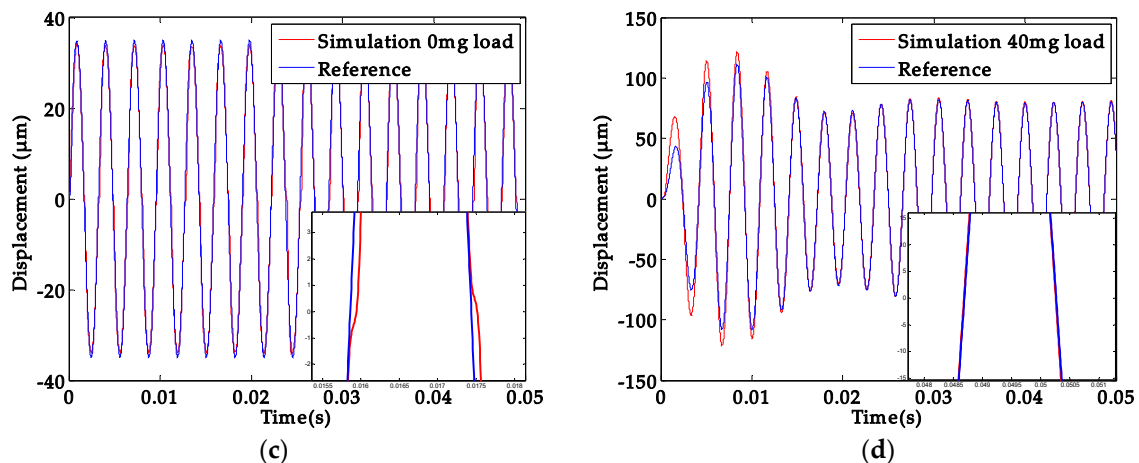


Figure 13. Displacement response simulation; (a) 0 mg load under 8 V (100 Hz); (b) 40 mg load under 8 V (100 Hz); (c) 0 mg load under 8 V (317 Hz); (d) 0 mg load under 8 V (317 Hz).

In Figure 13, when the 40 mg load is fixed on the platform, its first-order natural frequency decreased, which made the vibration state of platform closer to the resonance state. Although the loaded platform (40 mg) weakened its abnormal displacement response, this abnormal phenomenon was still obvious under the low frequency working state, which seriously affected the calibration accuracy across the full frequency range.

The displacement deviation induced by residual stress could be explained as follows. The fabricated beam exhibited an initial deflection $z_i(l_i)$ (Figure 14). When the stage moved to the zero position, more strain energy was needed to overcome the resistance of compressing beam and the axial load of PZT layer under the driving voltage, and therefore the needed energy from actuation costs more time than normal state, which shows an abnormal of movement through zero position.

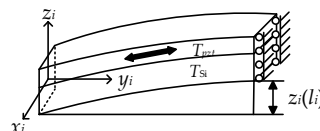


Figure 14. Each part diagram of L-shaped micro beam with the initial deflection $z_i(l_i)$.

5. Conclusions

In this study, the observed displacement response errors were investigated theoretically. It was concluded that both the displacement offset and increased frequency are caused by the residual stress from microfabrication, rather than the hysteresis of PZT materials. The initial deflection induced by residual stress makes the stage need more electrical energy to conquer the resistance of axial strain. Therefore, a good recalibration accuracy can be obtained by stress-free supporting beams or using the stimulus far from the zero point to calibrate the inertial sensors.

Author Contributions: R.H. and W.Z. structured and wrote the manuscript; W.Z. and B.P. provided resources; H.Y. and H.Z. performed the experiments; W.Z. planned the research concept and reviewed the manuscript. All authors have read and agreed to the published version of the manuscript.

Funding: This work was supported by the National Natural Science Foundation of China (Nos. 51505068, Nos. 51975107 and U1530132).

Conflicts of Interest: The authors declare no conflict of interest.

References

1. Olaf, D.; Georg, D.; Stefan, K. MEMS and FOG Technologies for Tactical and Navigation Grade Inertial Sensors—Recent Improvements and Comparison. *Sensors* **2017**, *17*, 567.
2. Singh, S.P.N.; Waldron, K.J. Attitude Estimation for Dynamic Legged Locomotion Using Range and Inertial Sensors. In Proceedings of the 2005 IEEE International Conference on Robotics and Automation, Barcelona, Spain, 18–22 April 2005; pp. 1663–1668.
3. He, J.; Zhou, W.; Yu, H. Structural Designing of a MEMS Capacitive Accelerometer for Low Temperature Coefficient and High Linearity. *Sensors* **2018**, *18*, 643. [[CrossRef](#)] [[PubMed](#)]
4. Zhou, W.; Peng, P.; Yu, H. Material Viscoelasticity-Induced Drift of Micro-Accelerometers. *Materials* **2017**, *10*, 1077. [[CrossRef](#)] [[PubMed](#)]
5. Zhou, W.; Chen, Y.; Peng, B.; Yang, H. Air Damping Analysis in Comb Microaccelerometer. *Adv. Mech. Eng.* **2015**, *6*, 373172. [[CrossRef](#)]
6. Dong, Y.; Zwahlen, P.; Nguyen, A.M. Ultra-high precision MEMS accelerometer. In Proceedings of the 2011 16th International IEEE Solid-State Sensors Actuators and Microsystems Conference (TRANSDUCERS), Beijing, China, 5–9 June 2011.
7. Emel'yantsev, G.I.; Dranitsyna, E.V.; Blazhnov, B.A. Test bed calibration of fog-based strapdown inertial measurement unit. *Gyroscopy Navig.* **2009**, *3*, 265–269. [[CrossRef](#)]
8. Sundaram, S.; Tormen, M.; Timotijevic, B. Vibration and shock reliability of MEMS: Modeling and experimental validation. *J. Micromech. Microeng.* **2011**, *21*, 045022. [[CrossRef](#)]
9. Link, T.; Simon, I.; Trachtler, M. A new self-test and self-calibration concept for micro-machined gyroscopes. In Proceedings of the TRANSDUCERS The 13th International IEEE Conference on Solid-State Sensors Actuators and Microsystems, Seoul, South Korea, 5–9 June 2005.
10. Puers, R.; Reynjtens, S. RASTA real acceleration for self test accelerometer: A new concept for self-testing accelerometers. *Sens. Actuators A* **2002**, *97–98*, 359–368. [[CrossRef](#)]
11. Aktakka, E.E.; Peterson, R.L.; Najafi, K. A 6-DOF piezoelectric micro vibratory stage based on multi-axis distributed-electrode excitation of PZT/Si unimorph T-beams. In Proceedings of the Solid-State Sensors, Actuators and Microsystems Transducers & Eurosensors XXVII: The 17th International Conference on IEEE, Barcelona, Spain, 16–20 June 2013.
12. Aktakka, E.E.; Najafi, K. A six-axis micro platform for in situ calibration of MEMS inertial sensors. In Proceedings of the 2016 IEEE 29th International Conference on Micro Electro Mechanical Systems (MEMS), Shanghai, China, 24–28 January 2016.
13. Edamana, B.; Slavin, D.; Aktakka, E.E. Control and estimation with threshold sensing for Inertial Measurement Unit calibration using a piezoelectric microstage. In Proceedings of the American Control Conference IEEE, Portland, OR, USA, 4–6 June 2014.
14. Zhou, W.; He, J.B.; Yu, H.J.; He, X.P. Analytical study of temperature coefficients of bulk MEMS capacitive accelerometers operating in closed-loop mode. *Sens. Actuators A* **2019**, *290*, 239–247. [[CrossRef](#)]
15. Papaioannou, G.; Exarchos, M.N.; Theonas, V. Temperature study of the dielectric polarization effects of capacitive RF MEMS switches. *IEEE Trans. Microw. Theory Tech.* **2005**, *53*, 3467–3473. [[CrossRef](#)]
16. Nadig, S.; Lal, A. In-Situ calibration Of MEMS inertial sensors for long-term reliability. In Proceedings of the 2018 IEEE International Reliability Physics Symposium, Burlingame, CA, USA, 11–15 March 2018.
17. Du, Y.J.; Yang, T.T.; Gong, D.D. High Dynamic Micro Vibrator with Integrated Optical Displacement Detector for In-Situ Self-Calibration of MEMS Inertial Sensors. *Sensors* **2018**, *18*, 2055. [[CrossRef](#)]
18. Yimnirun, R.; Wongsanmai, S.; Wongmaneerung, R. Stress and temperature dependent scaling behavior of dynamic hysteresis in soft PZT bulk ceramics. *Phys. Scr.* **2007**, *T129*, 184–189. [[CrossRef](#)]
19. Hues, S.M.; Draper, C.F.; Lee, K.P. Effect of PZT and PMN actuator hysteresis and creep on nanoindentation measurements using force microscopy. *Rev. Sci. Instrum.* **1994**, *65*, 1561–1565. [[CrossRef](#)]
20. Zhan, H.X.; Zhou, W.; Ran, L.Q. A high-resolution Optical Displacement Detection Method for Piezoelectric Micro Vibratory Stage. *IEEE Trans. Ind. Electron.* **2020**. [[CrossRef](#)]
21. Hao, R.; Peng, B.; Yu, H. Improved MEMS piezoelectric vibratory stage with reduced off-axis error. *J. Micro/Nanolithogr. MEMS MOEMS* **2020**, *19*, 015002. [[CrossRef](#)]
22. Hsueh, C.H. Modeling of Elastic Deformation of Multilayers Due to Residual Stress and External Bending. *J. Appl. Phys.* **2002**, *91*, 9652–9656. [[CrossRef](#)]

23. Aktakka, E.E.; Peterson, R.L.; Najafi, K. A 3-DOF piezoelectric micro vibratory stage based on bulk-PZT/silicon crab-leg suspensions. In Proceedings of the IEEE International Conference on Micro Electro Mechanical Systems, Taipei, Taiwan, 20–24 January 2013.
24. Saxena, S.; Sharma, R.; Pant, B.D. Design and development of guided four beam cantilever type MEMS based piezoelectric energy harvester. *Microsyst. Technol.* **2016**, *23*, 1–9. [[CrossRef](#)]
25. Wang, Z.; Matova, S.; Elfrink, R. A piezoelectric vibration harvester based on clamped-guided beams. In Proceedings of the IEEE International Conference on Micro Electro Mechanical Systems, Paris, France, 29 January–2 February 2012; pp. 1201–1204.
26. Dutta, S.; Imran, M.; Pandey, A. Estimation of bending of micromachined gold cantilever due to residual stress. *J. Mater. Sci.* **2014**, *25*, 382–389. [[CrossRef](#)]
27. Bao, M. *Analysis and Design Principles of MEMS Devices*; Elsevier: Amsterdam, The Netherlands, 2005; pp. 59–61.
28. Weinberg, M.S. Working equations for piezoelectric actuators and sensors. *J. Microelectromech. Syst.* **1999**, *8*, 529–533. [[CrossRef](#)]
29. Shepard, J.F.; Moses, P.J.; Trolier-McKinstry, S. The wafer flexure technique for the determination of the transverse piezoelectric coefficient (d_{31}) of PZT thin films. *Sens. Actuators A* **1998**, *71*, 133–138. [[CrossRef](#)]
30. Krejčí, P. The Preisach hysteresis model: Error bounds for numerical identification and inversion. *Discrete Contin. Dyn. Syst. Ser. S* **2012**, *6*, 101–119. [[CrossRef](#)]
31. Janaideh, M.A.; Rakheja, S.; Su, C.Y. An Analytical Generalized Prandtl–Ishlinskii Model Inversion for Hysteresis Compensation in Micropositioning Control. *IEEE-ASME Trans. Mechatron.* **2011**, *16*, 734–744. [[CrossRef](#)]
32. Badrakhan, F. Dynamic analysis of yielding and hysteretic systems by polynomial approximation. *J. Sound Vib.* **1988**, *125*, 23–42. [[CrossRef](#)]
33. Bashash, S.; Jalili, N. A Polynomial-Based Linear Mapping Strategy for Feedforward Compensation of Hysteresis in Piezoelectric Actuators. *J. Dyn. Syst. Meas. Control* **2008**, *130*, 031008. [[CrossRef](#)]
34. Yimnirun, R.; Laosiritaworn, Y.; Wongsanmai, S. Scaling behavior of dynamic hysteresis in soft lead zirconate titanate bulk ceramics. *Appl. Phys. Lett.* **2006**, *89*, 162901. [[CrossRef](#)]



© 2020 by the authors. Licensee MDPI, Basel, Switzerland. This article is an open access article distributed under the terms and conditions of the Creative Commons Attribution (CC BY) license (<http://creativecommons.org/licenses/by/4.0/>).